

## Metal partitioning after in situ filtration at deep-sea vents of the Lucky Strike hydrothermal field (EMSO-Azores, Mid-Atlantic Ridge, 37°N)

Cotte Laura <sup>1,2</sup>, Chavagnac V. <sup>3</sup>, Pelleter Ewan <sup>4</sup>, Laës-Huon A. <sup>5</sup>, Cathalot Cecile <sup>4</sup>,  
Dulaquais Gabriel <sup>1</sup>, Riso Ricardo <sup>1</sup>, Sarradin Pierre-Marie <sup>2</sup>, Waeles Mathieu <sup>1,\*</sup>

<sup>1</sup> Univ Brest, CNRS, IRD, Ifremer, LEMAR, F-29280, Plouzané, France

<sup>2</sup> Laboratoire Environnement Profond (LEP/EEP/REM), Ifremer, ZI de La Pointe Du Diable, CS 10070, 29280, Plouzané, France

<sup>3</sup> Laboratoire Géosciences Environnement Toulouse, GET UMR-CNRS 5563, Université de Toulouse, 31400, Toulouse, France

<sup>4</sup> Laboratoire Cycle Géochimique et Ressources (LCG/GM/REM), Ifremer, ZI de La Pointe Du Diable, CS 10070, 29280, Plouzané, France

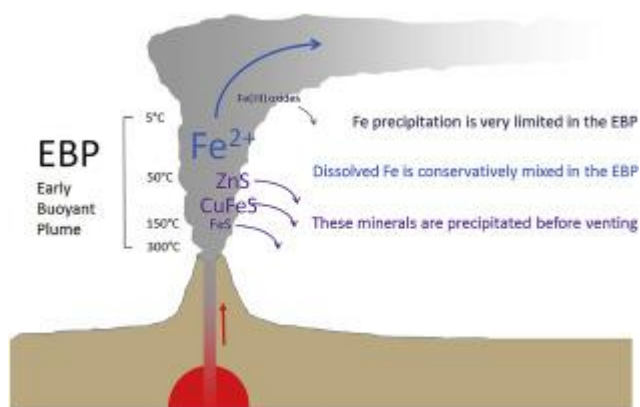
<sup>5</sup> Laboratoire Détection, Capteurs et Mesures (DCM/RDT/REM), Ifremer, ZI de La Pointe Du Diable, CS 10070, 29280, Plouzané, France

\* Corresponding author : Mathieu Waeles, email address : [waeles@univ-brest.fr](mailto:waeles@univ-brest.fr)

### Abstract :

Metal partitioning between the dissolved and particulate phases is still poorly constrained within the early mixing of hydrothermal fluids and deep seawater. In this study, in situ filtration has been used to collect early buoyant plume fluids. This has provided the unique opportunity to reassess precisely metal partitioning along the mixing gradient by limiting chemical exchange processes between the dissolved (<0.45 µm) and particulate (>0.45 µm) phases during sampling. We report on the partitioning of three major metals (Fe, Cu, Zn) in the early buoyant plume of six black and clear smokers from the Lucky Strike hydrothermal field (37°N, MAR; EMSO-Azores deep sea observatory). We show that chemical changes are limited in the warmest part of the plume [50–150°C, dMn > 40 µM; dilution factor (DF) of ~1–10 by NADW] as metal partitioning displays a chemical signature similar to the end-member one. However, as the dilution ratio between the hydrothermal fluid and North-Atlantic Deep-water (NADW) increases (4–50°C, dMn < 40 µM; DF of 10–100 by NADW), metal partitioning is affected by different precipitation and oxidation processes. Molar ratios normalized to Fe in the particles highlight the onset of Fe oxides formation, the precipitation of barite and the decreasing contribution of sulfide minerals (mainly Cu–Fe sulfides and sphalerite/wurtzite) along with fluid dilution.

## Graphical abstract



## Highlights

► Metal fate in early buoyant plumes of deep sea vents is poorly constrained. ► In-situ filtration indicates that chemical changes for Cu, Zn and Fe are limited. ► The main sulfide mineral phases precipitate before venting. ► The onset of Fe oxides formation occurs at high dilution.

**Keywords :** Deep-sea vents, Hydrothermal, Metal, Mixing gradient, Precipitation, In-situ filtration

## 30 1. Introduction

31 Hydrothermal circulation originates from the percolation and heating of seawater through the  
32 fractured oceanic crust (Alt, 1995). Since the first chemical analysis of vent plumes (Corliss et  
33 al., 1979; Edmond et al., 1979a, 1982), the geochemistry of hydrothermal fluids has been  
34 studied worldwide. The chemical composition of the end-member hydrothermal fluids is  
35 controlled by the extent of water/rock interactions, the occurrence of phase separation processes  
36 (Von Damm et al., 1995) and the degree of subsurface mixing with seawater (Edmond et al.,  
37 1979b). As a result, hydrothermal fluid can be highly enriched in alkali earth elements,  
38 transition metals and gas concentrations by up to a factor  $10^6$  compared to deep seawater. At  
39 the onset of mixing, the hydrothermal plumes include many different metal species, mostly  
40 reduced, inorganic and possibly organic species, that have been measured either in the dissolved  
41 and/or in the particulate phases (James & Elderfield, 1996; Field & Sherrell, 2000; Sarradin et  
42 al., 2008; Klevenz et al., 2011; Sands et al., 2012; Gartman et al., 2014; Findlay et al., 2015).  
43 The environmental changes due to the mixing between the hot and reduced hydrothermal fluid  
44 and the oxygenated deep seawater lead to the precipitation of metal-bearing particles.  
45 Polymetallic sulfides are the first to form, trapping mainly Fe(II) and other chalcophiles  
46 elements such as Cu and Zn (Feely et al., 1987; Trocine & Trefry, 1988; Mottl & McConachy,

1990; Klevenz et al., 2011; Breier et al., 2012) while, in the aging plume, the oxidation of the remaining dissolved Fe(II) later leads to the precipitation of iron oxyhydroxides (Rudnicki & Elderfield, 1993; Field & Sherrell, 2000). Such Fe-bearing oxyhydroxides are of great importance in the hydrothermal fluid–seawater mixing as they are efficient scavengers of oxyanions and rare earth elements (Feely et al., 1990a; b, German et al., 1990, 1991, Feely et al., 1994, 1998; Breier et al., 2012). Consequently, iron oxyhydroxides phases record the chemical composition of the distal hydrothermal plume along its dispersion in the water column.

The various precipitation processes were initially assumed to be exclusive to the discharge area and to limit drastically the input of hydrothermally sourced metal to the deep ocean (Mottl & McConachy, 1990; German et al., 1991). However, there are now increasing evidences that a significant fraction of metals such as Fe and Cu can be stabilized in seawater medium either as dissolved and/or as particulate organic complexes (Sander et al., 2007; Bennett et al., 2008; Toner et al., 2009; Hawkes et al., 2013) and/or as inorganic sulfide nanoparticles (Hsu-Kim et al., 2008; Yücel et al., 2011; Gartman et al., 2014). Hence, due to their low global density and size, these complexes and particles may be transported to long distances from the vent source and as such represent a significant export of metals of hydrothermal origin (e.g. Mn, Fe and likely Zn) to the ocean (Resing et al., 2015; Roshan et al., 2016; Fitzsimmons et al., 2017).

While the fate of metals, particularly Fe, has been extensively studied in distal hydrothermal plumes, i.e. hundreds to thousands of kilometers away from the discharge zone (e.g. Nishioka et al., 2013; Saito et al., 2013; Fitzsimmons et al., 2014; Hatta et al., 2015; Resing et al., 2015; Waeles et al., 2017), the behavior of metals in the early stage of buoyant hydrothermal plume formation, i.e. in the first centimeters to meters of venting, is still poorly documented (Sarradin et al., 2008; Klevenz et al., 2011; Gartman et al., 2014; Findlay et al., 2015). Yet, the early buoyant plume corresponds to the area where hydrothermally sourced metals are assumed to undergo extreme environmental changes due to the steep gradients of temperature, pH and oxygen concentrations operating below the meter scale. Tracking the fate of hydrothermal-derived metals within the buoyant plume is therefore critical to assess the net export flux of hydrothermal metal to deep seawater, especially because recent stable isotope studies have shown that reaction pathways involving metals such as Fe are much more complicated than thought hitherto (Rouxel et al., 2016; Toner et al., 2016; Klar et al., 2017).

The aforementioned studies of the buoyant hydrothermal plume have enabled to assess metal partitioning between the dissolved and the particulate fractions at  $< 2$  and  $< 0.2 \mu\text{m}$ . They confirmed that most of sulfide minerals are formed in close vicinity of the vent orifice (Sarradin et al., 2008; Klevenz et al., 2011; Gartman et al., 2014; Findlay et al., 2015). For example, Fe and Mn are mainly found as dissolved species ( $< 0.2 \mu\text{m}$ ), whereas Cu and Zn mostly occur as complexes forming particles of  $> 0.2 \mu\text{m}$  in size (Klevenz et al., 2011; Findlay et al., 2015). A further analysis of the  $< 0.2 \mu\text{m}$  fraction has finally highlighted the importance of sulfide nanoparticles in several hydrothermal vents from the Mid Atlantic Ridge (Gartman et al., 2014). Among these compelling studies, only one has performed *in situ* filtration, though with a higher filter porosity of  $2 \mu\text{m}$  (Sarradin et al., 2008) whereas the others have filtered samples once on board at  $0.2 \mu\text{m}$  (Klevenz et al., 2011; Gartman et al., 2014; Findlay et al., 2015). However, *in situ* filtration provides the opportunity to restrict drastically chemical changes between particle and dissolved phases, occurring once sampling is carried out and evidenced by precipitation of additional Cu-Zn sulfides and Fe oxides (Cotte et al., 2015). As a consequence, results from previous studies could be potentially biased by the precipitation and/or dissolution of particles which could occur after sampling. These biases have important implications for the fate of other elements that are particle reactive such as rare earth elements (Chavagnac et al., 2018).

Using *in situ* filtration, a previous survey on the partitioning of Fe, Cu and Zn has recently reported that 1) the precipitation of dissolved Fe is kinetically limited ( $< 10\%$ ) in the early

mixing (4–150°C) and 2) the resulting minerals should mainly correspond to Zn or Cu-rich sulfides mineral such as chalcopyrite or sphalerite/wurtzite (Waeles et al., 2017). However, the results presented for Cu and Zn in this previous study were limited to one smoker, i.e. Aisics (sampled in 2014). Here we report new data on Cu, Zn, Ba and Ca in the early mixing of six black and clear smokers of the Lucky Strike hydrothermal field (Aisics, Y3, Cypress, White Castle, Capelinhos and Sapin) with some of them being sampled at different times, i.e. Aisics (2015 and 2016), White Castle (2014, 2015 and 2016) and Capelinhos (2015 and 2016). A particular attention has been paid to the chemical processes which may affect the partitioning of metals upon mixing. Our objectives are thus to i) better understand the processes which drive metal partitioning along the mixing gradient and ii) explain the differences in buoyant plume fluid chemistry observed between the six smokers considered in this study.

## 2. Material and methods

### 2.1. Location of sampling

Sampling of buoyant hydrothermal plume fluids was performed at 6 vent smokers, i.e. Capelinhos, Y3, Aisics, White Castle, Cypress and Sapin, all of them located at the Lucky Strike hydrothermal field (LSHF, 37°17'N, Mid-Atlantic Ridge – MAR, **Figure 1**) during three oceanographic campaigns (Momarsat cruises in 2014, 2015 and 2016) on the R.V. *Pourquoi Pas?* and *l'Atalante*. The LSHF is situated at the summit of a central volcano, atop the axial magma chamber (AMC) located at ~ 3.4 kmbsf (Singh et al., 2006; Combier et al., 2015). Vents from the LSHF cluster around a fossil lava lake and are basalt-hosted systems (Humphris et al., 2002). Capelinhos, which was discovered in 2013, is located at ~ 1.5 km east of the Main LSHF (MLSHF, Escartin et al., 2015).

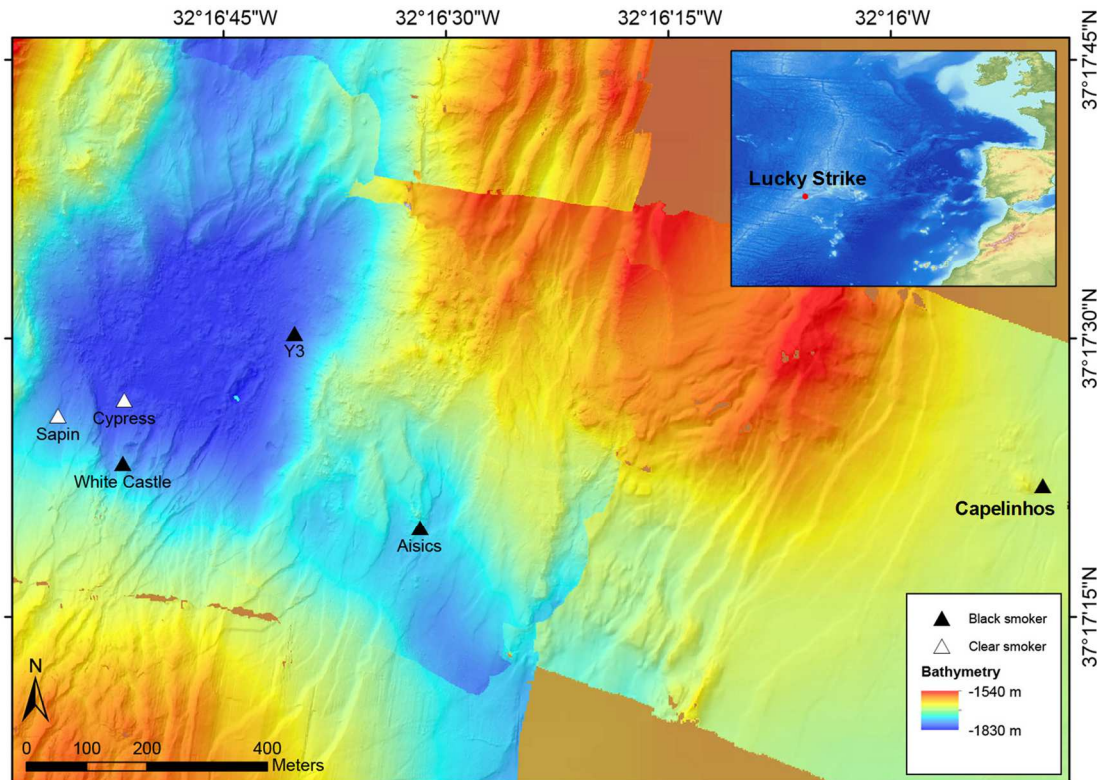


**Figure 1.** Map of the black and clear smokers sampled at the Lucky Strike hydrothermal vent field.

## 2.2. Fluid collection and sample processing

All equipment needed for sampling and filtration was rigorously washed with diluted hydrochloric acid (pH 2, Analytical Grade, Merck) and rinsed with ultrapure water (Milli-Q element system) prior to use. Samples from the mixing zone were filtered *in situ* using the PEPITO sampler implemented on the ROV Victor 6000 (Sarradin et al., 2007). The sampling strategy in the mixing zone has already been described in Cotte et al. (2015), Waeles et al. (2017) and Chavagnac et al. (2018). At each site, buoyant plume fluids were pumped into 2L-PVC/DEHP blood bags (Terumo, sterile treated by ethylene oxide, 1BDT200BM) with on-line filtration at 0.45  $\mu\text{m}$  (HATF, Millipore) from the seawater-dominated to the hydrothermal-dominated part of the mixing zone (4°C to ~ 150°C). Immediately after ROV Victor recovery onboard the research vessel, hydrothermal samples were processed in the chemical laboratory aboard (clean lab, Class 100 000, ISO 8). Each bag was then sub-sampled to carry out chemical analyses on-shore. All aliquots dedicated to the analysis of bulk dissolved metal concentrations were stored in acid-cleaned 15 mL-polypropylene tubes (Elkay). The 0.45- $\mu\text{m}$  porous membrane filters were dried by exerting suction to ensure that a minimum of seawater was left on their surface. Filters were stored in polystyrene petri-slides (Millipore). Aliquots and filters were then stored at 4°C until the onshore analyses of the dissolved (< 0.45  $\mu\text{m}$ ) and particulate concentrations (> 0.45  $\mu\text{m}$ ), respectively.

In addition to the PEPITO sampling, free inorganic sulfides ( $\Sigma\text{S} = \text{HS}^- + \text{S}^{2-} + \text{H}_2\text{S}$ ) were measured *in situ* using a chemical miniaturized analyzer (CHEMINI; Vuillemin et al., 2009). The *in situ* measurement is based on flow injection analysis with a colorimetric detection (methylene blue method; Le Bris et al. (2000)). A calibration of the analyzer was performed *in situ* at the beginning and at the end of each ROV dive using fresh standard solutions (respectively 0, 20, 50 and 100  $\mu\text{M}$ ) derived from a S(-II) stock solution (approx. 200 mM titrated every week). Hydrothermal samples were pumped without any filtration and the signal acquisition (~ 3 min) was initiated at the same time as the PEPITO sampling (the same titanium-Silicon cannula is used for both PEPITO and CHEMINI instruments). The chemical species analyzed corresponded to an operationally defined fraction of sulfides, herein called free inorganic sulfides. This fraction includes the dissolved and particulate sulfides in unfiltered samples that are labile enough to react with methylene blue at pH 4.7 (acetate buffer). Finally, the *in situ* concentration of dissolved oxygen was monitored during each sampling using an optode (Aanderaa) integrated in a flow cell in the sampling line/manifold. It is worth noting that the sampling frequency (0.033 Hz) of the optode, its response time and its internal correction for temperature does not allow to record the high variability of the mixing processes while sampling. Oxygen values were extrapolated according to the response time of the instrument. Oxygen concentrations reported here may therefore not represent exact values, but should rather be interpreted as maximal values.

## 2.3. Determination of dissolved and particulate metal concentrations

Concentrations for dissolved and particulate Fe, Cu, Zn, Ba, and Ca (dFe, pFe; dCu, pCu; dZn, pZn; dBa, pBa and dCa, pCa, respectively) as well as concentrations for particulate Mn, Mg and Sr (pMn, pMg and pSr) were determined using sector field inductively coupled plasma (ICP) mass spectrometry (Element 2, Thermofisher, Pôle Spectrométrie Océan – PSO –, Brest). Dissolved Mn and particulate sulfur concentrations (dMn and pS, respectively) were measured by ICP atomic emission spectrometry (Ultima 2, Horiba Jobin Yvon, PSO, Brest). For the analyses of the dissolved fraction, the samples were diluted 20-fold in a 2.5% nitric acid solution. Standards were prepared in a solution of seawater depleted of trace metals (Safe-

S, Geotrac reference sample, 2004) and diluted 20-fold in a 2.5% nitric acid solution but spiked with a multi-element solution (AccuStandard; 29 elements; 10 mg.L<sup>-1</sup>).

After the filter digestion procedure with 4 mL of nitric acid (65%, Suprapur, Merck) and 1 mL of hydrogen peroxide (30%, Suprapur, Merck), heating to 105°C for 4h (Cotte et al., 2015), the digestates were diluted in ultrapure water (final concentration: 2.5 % nitric acid). The standards for the particulate fraction were prepared from the aforementioned multi-element stock solution in a 2.5% nitric acid solution. In addition, other certified reference materials (CRM) used to check the digestion procedure on Fe, Cu and Zn included terrestrial sediment of volcanic origin enriched in Cu-sulfides (CCu-1c, Natural Resources Canada, NRCan) and Zn-sulfides (CZn-3, NRCan). Concentrations, recoveries and uncertainties obtained for the CRMs are provided in the supplementary information (**Table S1**). Dissolved and particulate concentrations were generally well above the limit of detection (LOD). Blanks, including ultrapure water processed in the PEPITO sampler, filter blanks and digestion blanks, were below the LOD, i.e. lower than 0.1 µM. Concentrations were determined with a precision generally better than 3% for Mn, Ba, Sr, 4% for Fe, Cu, Zn and 2% for Ca and Mg.

## 2.4. Salt precipitation artefact and corrections

Although a suction has been exerted on each filter once recovered on-board, a small volume of fluid can still be present in the filter and further evaporation of this fluid may provide a significant input of some major elements in the particulate fraction. To estimate this input, we considered that the occurrence of Mg in a filter was only due to fluid evaporation and salt precipitation. Then according to the content of Mg determined for each filter (typically in the range 5-10 µmol), and considering the position of each sample in the gradient (with dissolved Mg usually varying from 30 to 53 mM), we estimated the volume of evaporated fluid retained on each filter to 220±60 µL. We then calculated for each element (X) the molar ratio relatively to Mg obtained in the particulate fraction (pX:pMg). After comparison of the pX:pMg ratios with the fluid ratios (**Figure S1**), we found that the particulate Ca, Sr and Mn concentrations measured were essentially due to fluid evaporation. This salt effect was not important for Fe and Ba because they were found in large excess (two orders of magnitude) to the ratio estimated from salt precipitation. Particulate Fe and Ba data were however corrected from fluid evaporation (**Table 1**). pCu and pZn concentrations were not corrected because pX:pMg ratios estimated from fluid evaporation for these elements were much lower (5 orders of magnitude) than the measured ratios (**Figure S1**).

## 2.5. Statistical analysis

A principal component analysis (PCA) was used to determine groups of sites with fluids of similar chemical composition. Total concentrations (dissolved combined with particulate) of Fe, Cu, Zn and Ba (TFe, TCu, TZn and TBa) were normalized to TMn to overcome the dilution effect and were then averaged for each mixing gradient. Average values calculated for 2014 and 2015 at all sampling sites (including Tempo and Montsegur; Waeles et al. (2017)) were used for PCA. This multivariate PCA was performed in R using the RStudio software (v. 1.0.153, RStudio Inc.) and the FactoMineR package (Lê et al., 2008).



### 3. Results

#### 3.1. Characterization of the mixing gradient

Dissolved Mn (dMn) is used as a conservative tracer of the hydrothermal input in the mixing gradient owing to its slow reactivity with particles (Cowen et al., 1990; Field & Sherrell, 2000). Indeed, the removal rate of Mn (weeks to year) is considerably slower than the emplacement of neutrally buoyant plumes (on the order of tens of minutes) (Radford-Knoery et al., 1998). Dissolved Mn can thus be confidently used as a conservative tracer for the early mixing gradient sampled here (within 1.5 m after venting). Moreover, dissolved Mn being 4,000 times more enriched in hydrothermal fluid than in seawater, it provides much lower uncertainties than Mg for the determination of relatively high dilution factors. Based on dMn concentrations in hydrothermal end-members (Chavagnac et al., 2015, 2018a, 2018b; Leleu et al., 2015), the collected buoyant plume fluids broadly corresponds to a dilution factor of 2.3 to >100 of the hydrothermal fluid by deep seawater (i.e. North-Atlantic Deep-water (NADW) at this location; Zheng et al., 2016) corresponding to a temperature range from 4 to ~150°C. Concentrations for dissolved and particulate elements are summarized in **Table 1** (2014 and 2015) and **Table S2** (2016). Samples show enrichment in dMn up to  $4.10^5$  fold compared with the NADW (dMn ~ 0.5 nM; Yeats et al., 1992) which is typical of hydrothermal input at the early stage of mixing.

#### 3.2. Concentrations and partitioning in the early buoyant plume

##### *Fe, Cu and Zn*

Partitioning of Fe, Cu and Zn between the dissolved and particulate fractions in the buoyant plume shows similar pattern at the various sites. At each vent site, dFe is dominant when compared to pFe (**Figure 2**) with dFe concentrations ranging from 1–2  $\mu\text{M}$  to 100–200  $\mu\text{M}$  and pFe levels one-to-two orders of magnitude lower (range: < 0.5 to 14  $\mu\text{M}$ ). At Capelinhos, concentrations are particularly high with values up to 860  $\mu\text{M}$  and up to 32  $\mu\text{M}$ , for dFe and pFe respectively.

Unlike Fe, Cu and Zn are mainly found as particulate species. Concentrations for dCu and dZn never exceed 2  $\mu\text{M}$  and are generally in the range of 0.01 to 1  $\mu\text{M}$  at all vent sites (**Figure 2**, **Table 1**). In the particulate fraction, concentrations for Cu and Zn are in the same order of magnitude as that of Fe, ranging from < 0.1 to 17  $\mu\text{M}$ . Concentrations of pCu are relatively close to those of pFe and vary from site to site with maximum values at Capelinhos whereas pZn remain relatively constant between all sites.

A spatial variability among bulk dissolved and particulate Fe and Cu concentrations can be noticed from east to west of the LSHF (**Figure 2**). A gradient of concentration is indeed observed with a 6-fold increase of the dFe to dMn ratios ( $R_{\text{Fe}}$ ) from Sapin to Capelinhos ( $R_{\text{Fe}}$  from 0.72 to 4.65) as well as an eastward increase in bulk pFe and pCu levels (<5 to ~30  $\mu\text{M}$  and <1 to ~17  $\mu\text{M}$ , respectively). Therefore, Capelinhos displays the highest dFe concentrations (~2.5 mM for the hydrothermal end-member; Waeles et al., 2017) whereas Sapin exhibits the lowest dFe contents. Though to a lesser extent, vents located near the lava lake also show differences in fluid composition, evidenced in terms of dFe, pFe and pCu concentrations (e.g. Y3 and White Castle, **Figure 2**).

##### *Ba and Ca*

Partitioning of Ba between the dissolved and particulate fractions is very similar among all sites, with Ba being mainly in the dissolved fraction. Concentrations for dBa generally vary between 0.1  $\mu\text{M}$ , i.e. close to the concentration in seawater, and 30  $\mu\text{M}$ , excluding Sapin where concentrations up to 46  $\mu\text{M}$  were measured. On the contrary, the particulate pool exhibits systematically much lower concentrations than the dissolved pool. pBa does not exceed 1  $\mu\text{M}$ ,



1 except for Sapin where concentrations often reach  $\sim 2\text{-}3\ \mu\text{M}$ . One exception can be noticed at  
2 Aisics, where a concentration of  $\sim 2.5\ \mu\text{M}$  has been measured for pBa in the warmest part of  
3 the mixing gradient ( $d\text{Mn} = 96\ \mu\text{M}$ ;  $T \sim 130^\circ\text{C}$ ; **Table 1**). This anomaly could result from the  
4 collection of a chimney fragment enriched in barium, such as barite crystals, since the cannula  
5 was very close to the vent orifice when sampling. Because of the very low pBa levels measured  
6 at all vent sites, no particular trend can be observed for this element and the study of molar  
7 ratios in particles is needed to better examine the chemical changes involving pBa along the  
8 mixing gradient (see section 3.3.).

9 Calcium is a major constituent of hydrothermal fluid, with concentration level 2-3 times higher  
10 than in seawater. Dissolved Ca displays a conservative behavior in the mixing gradient as for  
11 the elements which occur essentially in the dissolved fraction, i.e. Ba and Fe (**Figure 3**).

12 The spatial variability of Ba and Ca concentrations among sites is not as marked as for Fe and  
13 Cu and only fluids from Capelinhos and Sapin can be distinguished from the 4 other sites  
14 (**Figure 3**). At Capelinhos, low concentrations of dBa and dCa are measured that do not exceed  
15  $12\ \mu\text{M}$  and  $13\ \text{mM}$  respectively, whereas vents from the MLSHF show concentrations of dBa  
16 and dCa up to  $46\ \mu\text{M}$  and  $20\ \text{mM}$  respectively. At Sapin, the difference in fluid chemistry arises  
17 from slightly higher dBa concentrations.

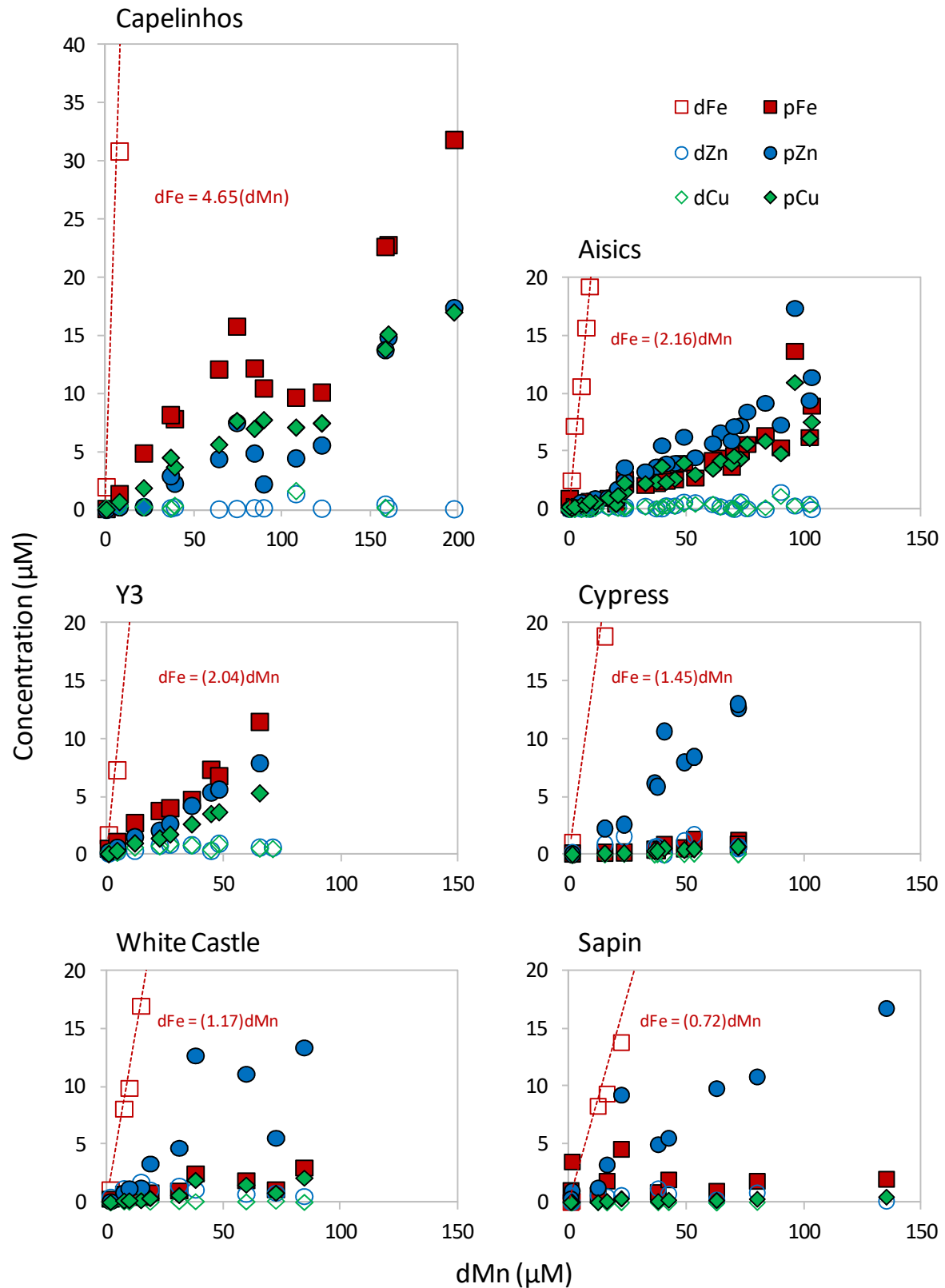


**Figure 2.** Dissolved and particulate concentrations of Fe, Zn and Cu at the main smokers of Capelinhos (2015), Aisics (2015), Y3 (2015), Cypress (2015), White Castle (2014) and Sapin (2014) all located at the LSHF. For the full scale plots of dFe, the reader is referred to the corresponding graphs and data published in Waeles et al. (2017). Red dashed lines show linear regression (forced to 0) between Fe and Mn with the corresponding dFe to dMn ratios ( $R_{Fe}$ ), also reported in (Waeles et al., 2017). Note the differences in dMn scale for Capelinhos.

**Table 1.** Dissolved and particulate concentrations of several elements in the early buoyant plume of Capelinhos, Aisics, Y3, Cypress, White Castle and Sapin from the Lucky Strike hydrothermal field (Momarsat 2014 and 2015). Note that Fe and Mn data have already been published in Waeles et al. (2017). Mean temperature recorded, picture taken during sampling, and elevation estimates of the sample collection from vent orifice (deduced from video recording) are also provided.

Vent	Date of sampling	Sample	Elevation cm	T °C	dMn μM	dFe μM	pFe μM	dCu μM	pCu μM	dZn μM	pZn μM	dBa μM	pBa μM	dCa mM
Capelinhos Black smoker 1665 m	20/04/2015	06602 A1	120	4.1	0.19	1.98	0.104	0.14	0.035	0.033	0.052	0.12		9.47
		06602 A2		9.0	7.62	30.9	1.38	0.360	0.703	0.319	0.251	0.68	0.029	9.59
		06602 A3		20	21.38	97.4	4.89	0.251	1.90	0.285	0.251	1.79	0.024	10.5
		06602 B1		34	38.91	187	7.83	0.378	3.70	0.244	2.28	3.19	0.019	10.8
		06602 B2	80	41	36.66	216	8.18	0.14	4.51	0.16	2.92	3.66	0.015	8.00
		06602 B3		51	63.96	300	12.1		5.62	0.061	4.40	5.01	0.021	10.9
		06602 C1		61	84.09	359	12.2	0.021	7.00	0.171	4.88	6.04	0.040	11.5
		06602 C2	50	73	74.11	367	15.8		7.67	0.106	7.50	5.87	0.041	9.66
		06602 C3		80	89.34	441	10.5		7.76	0.17	2.23	7.83	0.052	9.42
		06602 D1		89	107.6	512	9.69	1.65	7.12	1.379	4.46	8.54	0.042	11.1
		06602 D2	30	101	122.2	586	10.1		7.47	0.133	5.58	9.26	0.038	11.3
		06602 D3		112	159.9	741	22.8		15.1	0.130	14.9	10.2	0.097	12.6
		06602 E1		121	158.2	768	22.7	0.203	13.8	0.487	13.8	11.9	0.130	12.1
		06602 E3	20	139	197.1	857	31.9		17.0	0.087	17.4	11.7	0.059	12.5
Aisics Black smoker 1687 m	14/04/2015	02598 A1	150	5.3	1.08	2.50	0.171	0.019	0.079	0.117	0.110	0.56	0.013	9.07
		02598 A2		12	5.17	10.7	0.576	0.003	0.424	0.052	0.638	1.77	0.095	9.91
		02598 A3		17	11.06	23.6	0.746	0.110	0.616	0.273	0.972	4.09	0.010	10.4
		02598 B1	90	31	19.94	41.6	0.478	1.01	0.451	1.33	0.696	7.22	0.003	11.5
		02598 B2		41	23.67	52.8	2.19	0.205	1.53	0.282	2.48	7.85	0.044	12.0
		02598 B3		47	23.60	60.7	2.62	0.117	2.30	0.081	3.64	9.50	0.052	10.2
		02598 C1	70	57	37.16	89.1	2.24	0.112	2.39	0.066	3.70	12.3	0.045	13.8
		02598 C2		73	48.79	111	3.98	0.493	4.03	0.663	6.27	15.0	0.038	14.9
		02598 C3		68	44.92	98.9	2.58	0.280	2.63	0.325	4.01	14.1	0.039	14.1
		02598 D1		55	39.43	90.7	3.35	0.228	3.73	0.060	5.53	13.2	0.004	13.9
		02598 D2	35	97	64.33	146	4.44	0.192	4.22	0.254	6.66	19.0	0.063	16.6
		02598 D3		108	72.87	166	5.03	0.607	4.39	0.683	7.26	14.4	0.084	17.5
		02598 E1	30	121	83.39	195	6.38	0.169	5.92	0.003	9.21	21.1		18.5
		02598 E2		133	95.97	221	13.7	0.325	11.0	0.323	17.4	23.3	2.53	17.9
		02598 E3	20	154	102.2	230	6.17	0.400	6.16	0.487	9.43	23.7	0.097	19.6

Table 1. (continued).

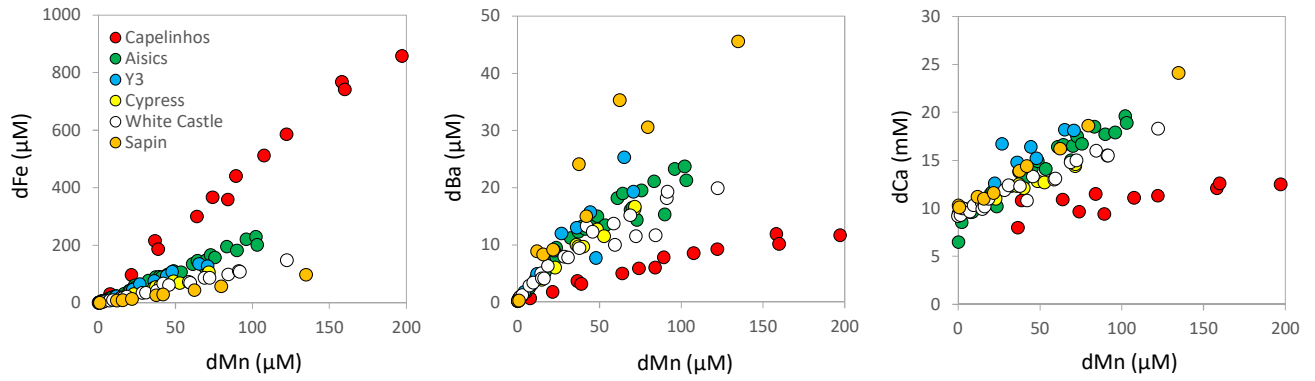
Vent	Date of sampling	Sample	Elevation	T	dMn	dFe	pFe	dCu	pCu	dZn	pZn	dBa	pBa	dCa
			cm	°C	μM	μM	μM	μM	μM	μM	μM	μM	μM	mM
Aisics Black smoker 1689 m	21/04/2015	07603 A1	60	5.0	0.19	0.40	1.00	0.007	0.217	0.013	0.046	0.20	0.043	6.49
		07603 A2		9.6	2.31	7.21	0.284	0.009	0.215	0.093	0.208	0.93	0.008	8.55
		07603 A3		21	7.26	15.7	0.392	0.020	0.370	0.130	0.221	2.47	0.004	9.92
		07603 B1		29	8.72	19.3	0.716	0.017	0.731	0.035	0.111	3.10	0.006	9.62
		07603 B2	40	39	16.67	31.9	0.977	0.105	1.01	0.249	1.03	5.18	0.012	10.5
		07603 B3		45	20.75	42.4	1.22	0.106	1.23	0.183	1.78	6.89	0.014	11.7
		07603 C1		56	32.39	76.6	2.09	0.212	2.26	0.303	3.28	11.2	0.021	12.3
		07603 C2		66	41.28	89.1	2.44	0.300	2.37	0.344	3.96	12.8	0.030	13.2
		07603 C3	30	89	69.05	124	3.66	0.099	3.96	0.158	5.95	16.1	0.013	15.0
		07603 D1		78	53.60	107	2.74	0.463	3.03	0.613	4.49	13.4	0.028	14.1
		07603 D2	20	93	61.10	135	4.23	0.491	3.51	0.434	5.71	18.2	0.157	16.4
		07603 D3		103	70.19	149	4.67	0.067	4.62	0.017	7.19	16.5	0.050	16.5
		07603 E1	15	112	75.68	158	5.63	0.078	5.68	0.078	8.45	19.5	0.057	16.7
		07603 E2		128	89.97	182	5.33	1.15	4.83	1.49	7.32	15.3	0.059	17.7
		07603 E3	10	138	103.1	202	8.93		7.57	0.007	11.4	21.3	0.095	18.9
Y3 Black smoker 1726 m	25/04/2015	10606 A1	120	5.0	0.65	1.70	0.529	0.159	0.065	0.124	0.233	0.67	0.054	9.54
		10606 A2		10	4.26	7.31	1.12	0.189	0.341	0.273	0.613	1.82	0.085	9.61
		10606 A3		20	11.78	22.9	2.76	0.638	0.996	0.354	1.53	4.91	0.047	10.4
		10606 B1	90	32	22.43	46.2	3.79	0.753	1.41	0.800	2.09	8.99	0.033	12.6
		10606 B2		35	26.88	65.1	4.04	0.931	1.75	0.888	2.68	12.0	0.013	16.7
		10606 B3	50	50	36.17	75.5	4.75	0.805	2.65	0.841	4.24	13.0	0.073	14.8
		10606 C1		60	44.45	93.4	7.35	0.438	3.53	0.344	5.40	15.7	0.022	16.4
		10606 C2		69	47.85	108	6.81	0.912	3.68	0.968	5.65	7.69	0.068	15.2
		10606 C3		80	70.83	128		0.494		0.623		19.3		18.1
		10606 D1	30	89	65.22	136	11.5	0.549	5.32	0.636	7.92	25.3	0.090	18.2

Table 1. (continued).

Vent	Date of sampling	Sample	Elevation	T	dMn	dFe	pFe	dCu	pCu	dZn	pZn	dBa	pBa	dCa
			cm	°C	μM	μM	μM	μM	μM	μM	μM	μM	μM	mM
Cypress Clear smoker 1738 m	23/04/2015	08604 A1	40	5.4	0.92	1.03	0.109	0.002	0.017	0.150	0.032	0.33	0.017	9.32
		08604 A2		14	14.76	18.9	0.173	0.038	0.126	0.924	2.27	3.91	0.010	10.2
		08604 A3	15	20	40.10	58.3	0.848	0.007	0.565	0.055	10.7	9.68	0.102	12.1
		08604 B1		25	22.96	29.9	0.197	0.093	0.135	1.58	2.61	6.00	0.007	11.0
		08604 B2	10	37	35.97	52.1	0.451	0.035	0.334	0.617	6.18	10.0	0.010	12.3
		08604 B3		50	37.15	55.0	0.402	0.064	0.317	0.691	5.90	9.74	0.009	12.5
		08604 C1	5	57	48.62	74.9	0.552	0.070	0.413	1.18	8.00	12.7	0.017	12.8
		08604 C2		64	71.72	107	1.21	0.055	0.691	0.671	12.7	16.7	0.107	14.6
		08604 C3		76	71.49	103	0.877	0.047	0.688	0.571	13.0	16.3	0.023	14.4
		08604 D1	2	95	52.80	69.2	1.29	0.106	0.483	1.71	8.47	11.5	0.186	12.7
White Castle Clear smoker 1708 m	28/07/2014	11586 A1	120	6.1	1.44	1.15	0.35	0.020	0.056	0.520	0.125	0.94	0.026	9.31
		11586 A2		13	7.22	8.13	0.79	0.097	0.180	1.26	0.892	2.86	0.091	9.65
		11586 A3	60	23	14.49	17.0	0.50	0.260	0.199	1.81	1.31	5.05	0.037	10.6
		11586 B1		32	9.46	9.92	0.76	0.069	0.211	0.956	1.25	3.39	0.043	10.3
		11586 B2	30	42	18.44	22.1	0.89	0.078	0.395	1.13	3.38	6.31	0.028	11.0
		11586 B3		45	30.83	35.2	1.05	0.129	0.658	1.47	4.74	7.78	0.072	12.4
		11586 C1		61	72.27	87.1	1.15	0.157	0.855	0.849	5.61	11.5	0.107	15.0
		11586 C2	20	76	59.53	70.1	1.94	0.104	1.56	0.758	11.1	10.0	0.098	13.1
		11586 C3		99	37.81	41.5	2.52	0.123	1.97	1.12	12.7	9.41	0.169	12.3
		11586 D1	15	125	84.36	98.9	3.04	0.060	2.16	0.567	13.4	11.7	0.119	16.0

Table 1. (continued).

Vent	Date of sampling	Sample	Elevation cm	T °C	dMn μM	dFe μM	pFe μM	dCu μM	pCu μM	dZn μM	pZn μM	dBa μM	pBa μM	dCa mM
White Castle Clear smoker 1708 m	18/04/2015	04600 A1		4.6	0.02	0.56	0.551	0.02	0.025	0.26	0.149	0.23	0.307	9.20
		04600 A2		20	16.11	17.9	1.18	0.05	0.407	0.42	3.90	4.11	0.087	10.2
		05601 A1	90	6.5	2.87	2.93	1.11	0.02	0.145	0.24	0.867	1.23	0.330	10.0
		05601 A2		20	14.78	17.6	2.32	0.06	0.897	0.31	7.57	4.18	0.019	9.93
		05601 A3	70	33	28.48	34.4	0.419	0.09	0.251	0.61	2.25	7.94	0.351	11.9
		05601 B1		49	45.80	61.5	1.35	0.30	0.828	1.86	7.19	12.3	0.085	13.3
		05601 B2	35	59	42.16	66.8	1.37	0.22	0.92	1.27	7.96	13.3	0.031	10.8
		05601 B3		69	58.68	72.8	2.14	0.14	1.16	0.65	10.9	13.7	0.070	13.0
		05601 C1	15	93	68.85	87.7	2.71	0.07	1.34	0.14	12.1	15.2 <sup>#</sup>	0.100	14.8 <sup>#</sup>
		05601 C2	10	100	122.35	148	4.96	0.24	2.35	1.17	19.2	19.9 <sup>#</sup>	0.119	18.3 <sup>#</sup>
		05601 C3		117	91.15	111	3.53	0.40	1.72	2.11	15.4	18.2 <sup>#</sup>	0.129	15.5 <sup>#</sup>
		05601 D1	3	113	91.67	108	4.25	0.12	2.27	0.57	20.6	19.3 <sup>#</sup>	0.091	15.5 <sup>#</sup>
Sapin Clear smoker 1718 m	21/07/2014	05580 A1	25	5.1	0.79	0.15	3.55	0.009	0.082	0.046	1.04	0.28	1.668	10.1
		05580 A2		4.5	0.30	0.05	1.09	0.013	0.044	0.064	0.360	0.22	0.796	10.3
		05580 A3	15	11	11.87	8.37	0.67	0.017	0.040	0.659	1.31	8.90	0.493	11.2
		05580 B1		18	37.49	26.7	0.92	0.019	0.137	1.24	5.05	24.1	0.534	13.9
		05580 B2	5	31	62.40	43.8	1.02	0.013	0.220	0.271	9.89	35.3	0.712	16.2
		05580 B3		45	79.67	57.4	1.88	0.055	0.333	0.889	10.9	30.6	1.913	18.6
		05580 C1	3	49	134.8	98.1	2.05		0.506	0.159	16.8	45.6	2.664	24.1
		05580 C2		70	21.82	13.9	4.65	0.034	0.367	0.659	9.33	9.17	1.965	11.6
		05580 C3		80	15.71	9.42	1.89	0.011	0.142	0.543	3.30	8.30	0.598	11.0
		05580 D1	1	90	41.94	28.9	2.00	0.038	0.247	0.784	5.60	15.0	0.805	14.4



**Figure 3.** Concentrations of dFe, dBa and dCa as a function of dMn over the 6 vent sites sampled at the LSHF. Discrepancies in concentrations at Capelinhos compared to the sites from MLSHF are easily noticeable.

### 3.3. Molar ratios in hydrothermal particles

For each site, molar ratios of pZn/pFe, pCu/pFe and pBa/pFe against dMn concentrations are presented in **Figure 4**. These ratios remain relatively constant in the hottest part of the gradient, i.e. at dMn concentrations above  $\sim 40 \mu\text{M}$ . In the coldest part, both pZn/pFe and pCu/pFe ratios promptly decrease while pBa/pFe ratios increase along the mixing gradient towards the NADW-dominated part of buoyant plume. These changes of molar ratios are of 1-2 order of magnitude.

Although the different sites display similar trends, strong discrepancies are observed between sites in term of molar ratios. These discrepancies are also clearly observed by plotting pCu/pFe versus pZn/pFe for dMn concentrations above  $\sim 40 \mu\text{M}$  (**Figure 5**).

- At Aisics, Y3 and Capelinhos, the pZn/pFe ratios are in the range 1.0-1.7, 0.3-0.8 and 0.2-0.7 respectively. The pZn/pFe are relatively high at White Castle, Sapin and Cypress. The observed ranges at these 3 sites of 4-6, 3-10 and 6-15, respectively, are all significantly above 1 indicating that sphalerite/wurtzite ( $\text{ZnS}$ ) should dominate other typical minerals containing Fe (e.g.  $\text{CuFeS}_2$  or  $\text{Fe}_{1-x}\text{S}$ ).
- At Sapin the molar ratios of pCu/pFe are relatively low ( $\sim 0.1$ -0.3) compared to the other sites ( $\sim 0.4$  to 1.1). In the case of Capelinhos, Y3 and Aisics, pCu/pFe ratios are close to 1 and indicate that chalcopyrite ( $\text{CuFeS}_2$ ) should be the dominant mineral at these sites.

The differences between vent sites are less clear for the pBa/pFe ratios. However, the sites exhibiting high pZn/pFe ratios (White Castle, Sapin and Cypress) display also the highest pBa/pFe molar ratios (**Figure 6**). This is particularly obvious at Sapin which has the most Ba-enriched fluids of the MLSHF vent sites studied (**Figure 3**).

Overall, the variability observed for the different molar ratios between each vent sites likely arises from differences in the chemical composition of the end-member fluids as well as the impact of NADW. Such variability reflects the preferential occurrence of specific minerals (i.e. sphalerite/wurtzite or chalcopyrite/isocubanite) within each mixing gradient.



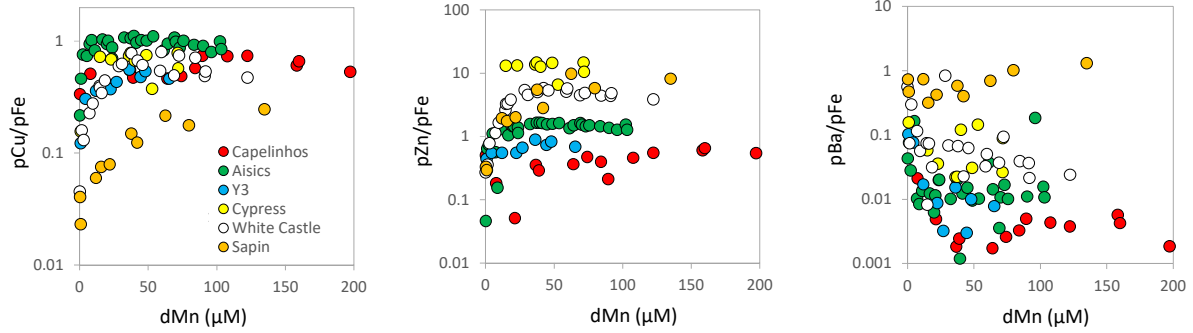


**Figure 4.** Molar ratios  $pZn/pFe$ ,  $pCu/pFe$  and  $pBa/pFe$  in particles versus  $dMn$  over the 6 vent sites sampled at the LSHF.

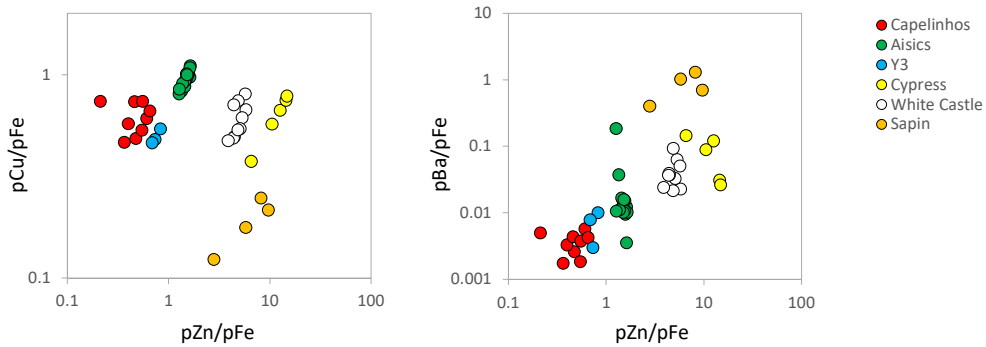


**Figure 5.**  $pCu/pFe$  and  $pZn/pFe$  molar ratios as a function of  $pZn/pFe$  molar ratio for sample with  $dMn$  concentrations above  $40 \mu M$  over the 6 vent sites sampled at the LSHF.

## 4. Discussion

### 4.1. Inter-site variability of dissolved and particulate metal concentrations

Variabilities in the end-member fluid chemical composition have been recently observed between Capelinhos and the MLSHF but also among sites within the MLSHF (Leleu et al., 2015; Chavagnac et al., 2018a; Leleu, 2017). These authors highlighted east-west differences in  $dFe$  concentrations with much higher levels at Capelinhos ( $Fe \sim 2-3 \text{ mM}$ ) compared to the MLSHF ( $120-600 \mu M$ ). Variabilities in  $dFe$  concentrations among the MLSHF sites are also reported with higher levels at Cypress, Y3 and Aisics ( $575 \mu M$ ,  $563 \mu M$  and  $522 \mu M$ , respectively) than at White Castle ( $407 \mu M$ ) or Sapin ( $121 \mu M$ ) (Leleu, 2017). These spatial variability in  $Fe$  concentrations has been explained by differences in subsurface processes (Chavagnac et al., 2018a; Chavagnac et al., 2015; Leleu, 2017).

These east-west  $dFe$  differences in the end-members fluids match the spatial variability observed for dissolved and particulate metal concentrations (i.e.  $dFe$ ,  $pFe$  and  $pCu$  concentrations, **Figure 2**) in direct link with the hydrothermal discharge and plumbing system at the LSHF. Inside the MLSHF, Barreyre et al. (2012) showed a clear disparity between the east and west with faults network flanking the graben. Escartin et al. (2015) later showed that Capelinhos, located East of the axial magma chamber edge, is likely associated to flow along a permeable fault that may root at the main upwelling zone with hydrothermal fluid less prone to subsurface dilution processes or conductive cooling.

Inter-site variabilities of the fluid chemical composition are also clearly highlighted by a PCA (**Figure 6**). 85% of the inter-site variability can be explained by the chemical parameters considered to build the PCA. The first axis of the PCA accounts for nearly 58% of the variability

in fluid composition and separates the most Fe-Cu-enriched sites (Capelinhos, Aisics and Y3) to sites enriched in Zn and Ba (Montsegur, Tempo and Sapin). The second axis (27%) separates Cypress and White Castle from the other sites because of higher TMn concentrations, i.e. lower metal to TMn ratios. From this PCA, four groups can be identified: 1) Capelinhos, 2) Aisics and Y3, 3) Cypress and White Castle and 4) Sapin. Interestingly, Montsegur and Tempo split from Aisics, despite their close localization in the field. We suppose that the sampling of diffuse and auxiliary smokers at these two sites, instead of main black smokers, lead to fluids with chemical properties closer to those of Sapin. The most striking changes are observed in the mixing being between Capelinhos and sites from the MLSHF (**Figure 2** and **Figure 6**). Weak differences in bulk concentrations of metals can also be noticed between sites from the MLSHF. These features are discussed in the two following sections.

#### 4.1.1. Differences between Capelinhos and MLSHF

A large part of the differences we observe in term of chemical composition of the early buoyant plume between Capelinhos and the other sites is related to the specific chemical composition of each fluid end-member. For instance, Capelinhos fluid end-member, which exhibits the highest dFe concentrations of the MLSHF, leads to very high concentrations in both the dissolved and the particulate Fe in the early buoyant plume compared to the other vent sites (**Figure 2** and **Figure 3**). The primary chemical features of the hydrothermal fluid, e.g. Fe concentrations, are therefore still noticeable after discharge over a large part of the mixing gradient (50-150°C). This is likely due to the kinetically limited chemical changes affecting Fe in this area (Waeles et al., 2017) which can be tracked by a relatively high and stable dFe/dMn ratio upon mixing.

Capelinhos early buoyant plume also exhibits the highest concentrations for particulate Cu compared to sites from the MLSHF. This feature could be explained by differences in the end-member fluid temperature between Capelinhos and MLSHF. At Capelinhos, the fault configuration enables a direct outflow of fluid with temperature greater than 300°C (Escartin et al., 2015; Chavagnac et al., 2018a). Dissolved Cu, which is very sensitive to variations of temperature, can reach the discharge zone before its massive precipitation at temperature below 300°C. Capelinhos end-member fluid could hence be initially rich in dissolved Cu but this dCu would immediately precipitate within the chimney after exiting the seafloor. This hypothesis is consistent with the higher pCu concentrations observed in the warmest part of the mixing gradient (> 100°C) at Capelinhos compared to MLSHF vents. Fluids emanating from the MLSHF have likely undergone important Cu precipitation and loss processes before discharge, explaining their generally lower concentrations measured for pCu in the early buoyant plume.

#### 4.1.2. Differences between sites from the MLSHF

Surrounding the lava lake, vent sites from the MLSHF are sustained by the same deep source that of Capelinhos but their end-member fluids have undergone chemical equilibration at shallower depth due to a higher residence time of hydrothermal fluid in the upflow zone (Chavagnac et al., 2018a). The numerous axial faults and fissures around the lava lake can promote percolation of seawater into the crust (Humphris et al., 2002; Barreyre et al., 2012). These seepages lead to a subsequent mixing of the hydrothermal fluid with seawater and/or to conductive cooling under the seafloor resulting in 1) the precipitation of Fe-Cu-enriched sulfides particles before the fluid discharge and 2) lower concentrations of Fe and probably of Cu in the end-members fluids (Leleu, 2017; Chavagnac et al., 2018a). As previously mentioned, the differences of chemical composition between sites from the MLSHF (**Figures 2, 4 7**) are likely related to the chemical composition of each end-member, itself affected by the depth of

the reaction zone as well as by the conductive cooling associated with different channeling pathways prior to venting at the deep seafloor. Note that pZn concentrations remain similar at the five vent sites considered. This is in agreement with the limited effect of temperature on Zn solubility in hydrothermal fluids (Seyfried & Ding, 1995; Metz & Trefry, 2000). Overall, our results show that the geochemical composition of the early buoyant plume is mainly driven by the end-member fluid signature itself and, thus, by subsurface processes over a large part of the mixing gradient (typically  $T > 50^{\circ}\text{C}$ ). Therefore, the mixing of hydrothermal fluids with seawater in this area of the gradient is mainly conservative. This is due to the relative slow kinetics of the geochemical reactions as compared to the high mixing velocity. Changes in the chemical composition of the fluids occurring at a more advanced dilution state ( $T < 50^{\circ}\text{C}$ ) are discussed in the following sections.

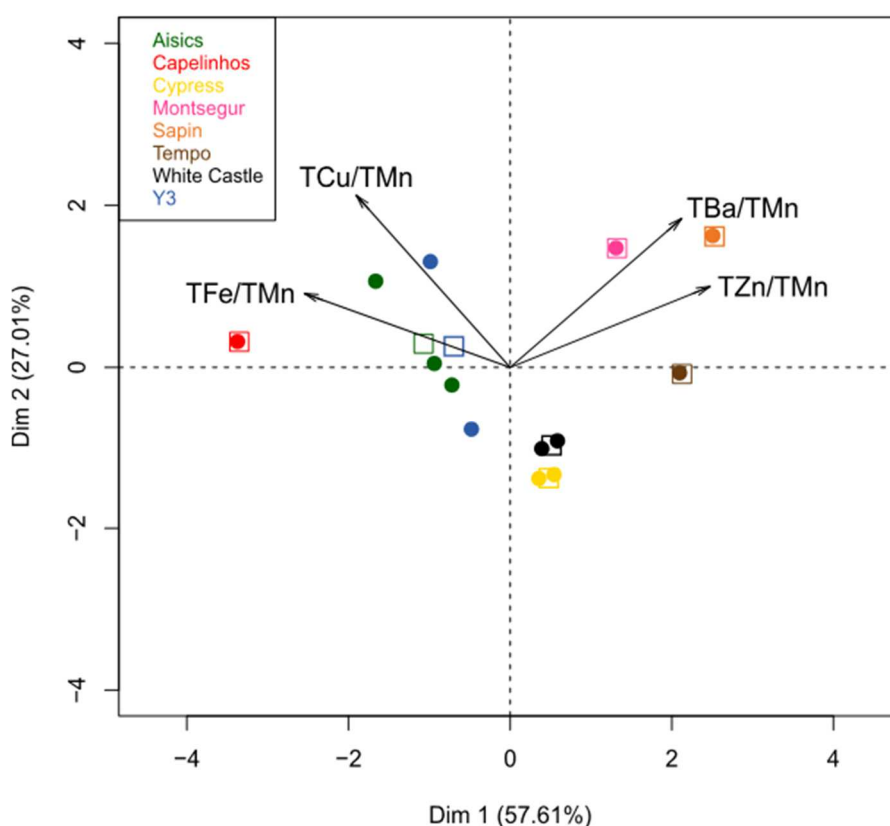


**Figure 6.** PCA showing the different groups of sites with similar chemical properties. Total concentrations of Fe, Cu, Zn and Ba normalized to total Mn and then averaged at each mixing gradient are used for PCA. Only fluids emanating from the main black smokers are taken into account except at Montsegur and Tempo (diffused and auxiliary smokers). Each point depicts one mixing gradient (for 2014 and 2015). Squares symbolize the average of all mixing gradients at each vent site.

## 4.2. On the chemical processes occurring upon mixing

The *in situ* filtration method used in this study provided several insights on the chemical processes occurring at the onset of hydrothermal plume formation. These processes consist essentially in precipitation reactions which are examined using measured molar ratios of particles. The pZn, pCu and pBa data were normalized to pFe because of the involvement of Fe in several chemical processes all along the mixing gradient such as its inclusion in polymetallic sulfides (Feely et al., 1987; Trocine & Trefry, 1988; Mottl & McConachy, 1990; Klevenz et al., 2011; Breier et al., 2012) and the formation of Fe-oxyhydroxides (Rudnicki & Elderfield, 1993; Field & Sherrell, 2000). Two antagonistic behaviors are observed throughout the mixing gradient when plotting molar ratios against the dMn concentrations (**Figure 4**). On one hand, pCu/pFe and pZn/pFe molar ratios decrease in the coldest part of the mixing. On the other hand, pBa/pFe molar ratios increase with the fluid dilution.

The pCu/pFe and pZn/pFe ratios, which remain relatively constant in the hottest part of the studied mixing gradient, promptly decrease by about 1 order of magnitude for dMn concentrations greater than 40  $\mu\text{M}$  (**Figure 4**). Different precipitation processes involving Fe can explain this chemical feature: the precipitation of pyrite and/or the precipitation of Fe-oxyhydroxides. As the kinetic of pyrite formation is very slow in the mixing zone ( $\sim 2 \text{ pM} \cdot \text{min}^{-1}$ ; Graham & Ohmoto, 1994; Rickard, 1997), we rather relate the decreasing pZn/pFe and pCu/pFe ratios to a progressive oxidation of Fe(II) to Fe(III) under more alkaline and oxidizing conditions. Such mechanism will lead as the dilution progresses, to the precipitation of Fe-oxyhydroxides in the coldest part (4 to  $\sim 50^\circ\text{C}$ ) of the mixing gradient (Mottl & McConachy, 1990; Rudnicki & Elderfield, 1993; Field & Sherrell, 2000). According to Millero et al., (1987), the Fe(II) oxidation rate has partial orders of 1 and 2 with respect to dissolved oxygen ( $\text{O}_2$ ) and  $\text{OH}^-$  concentrations. Changes in these parameters over the mixing gradients of MLSHF are shown in **Figure 7**. Over the mixing zone studied,  $\text{O}_2$  is at relatively high concentrations and its variations are limited (usually in the range 100–300  $\mu\text{M}$ ). pH changes are however much more important, increasing from  $\sim 5$  to above 7 at all vent sites (**Figure 7**), and must be responsible of the onset of Fe(II) oxidation. Indeed, using equation 1 (Millero et al. 1987) and the typical chemical conditions observed between  $50^\circ\text{C}$  and  $5^\circ\text{C}$  for MLSHF vents (**Table 1** and **Table S3**), the kinetic of Fe(II) oxidation can be estimated to vary from  $\sim 5 \text{ pM} \cdot \text{min}^{-1}$  at  $50^\circ\text{C}$  to  $\sim 1000 \text{ pM} \cdot \text{min}^{-1}$  at  $5^\circ\text{C}$ . These rates are much higher than pyrite formation, i.e.  $\sim 2 \text{ pM} \cdot \text{min}^{-1}$  especially in the colder part of the mixing gradient.

$$\frac{-d[\text{Fe(II)}]}{dt} = k[\text{Fe(II)}][\text{O}_2][\text{OH}^-]^2 \quad (\text{Eq. 1})$$

Besides Fe oxidation/precipitation processes, the settling out of Zn and/or Cu-sulfide particles through aggregation can also partly explain the decrease of both pZn/pFe and pCu/pFe ratios. Indeed, the study by Feely et al. (1990a) clearly indicates that aggregation of Zn and Cu sulfide particles after venting can produce aggregates of hundreds of  $\mu\text{m}$ . Moreover a differential sedimentation occurs between the large and dense sulfide minerals on one hand and small Fe-oxyhydroxides on the other hand. This differential sedimentation leads to a decreasing contribution of the sulfide to the particle load along the mixing gradient.

The increase of the pBa/pFe molar ratio with the fluid dilution and especially at Mn concentrations  $< 40 \mu\text{M}$  (**Figure 4**), may reflect pBa contribution as barite crystals precipitation as suggested by previous studies (Feely et al., 1987; Breier et al., 2012). This latter process is thought to be more important than precipitation of Fe as oxyhydroxides in this specific area of the mixing gradient. Precipitation of barite minerals is predicted to preferentially occur between  $\sim 25$  and  $100^\circ\text{C}$  (Breier et al., 2012). This is consistent with the trend we observe here (Figure

4) and with secondary electron micrograph observation of particles collected within the buoyant plume of White Castle (Chavagnac et al., 2018b).

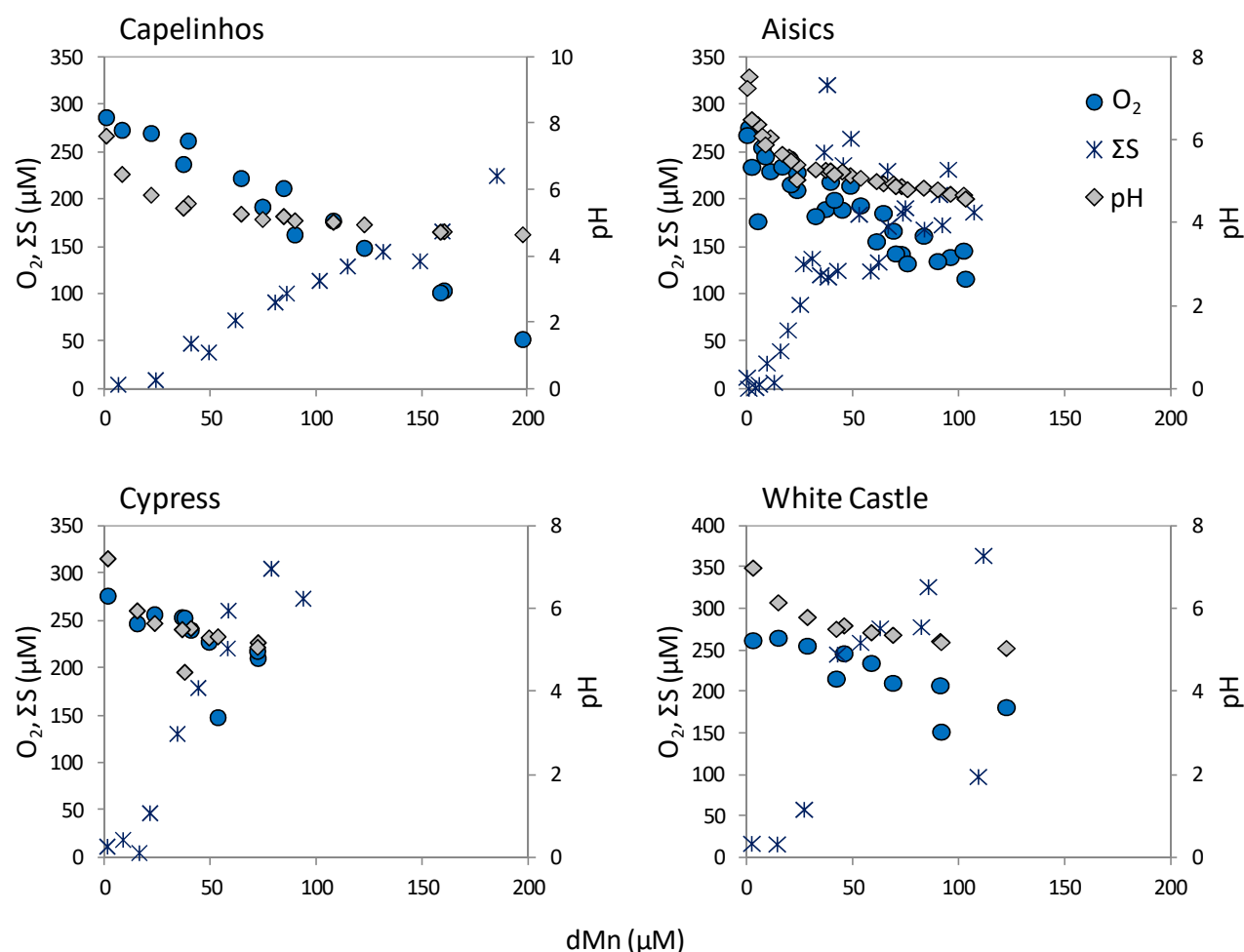


**Figure 7.** *In situ* chemical parameters (O<sub>2</sub>, ΣS) and pH (measured on board) as a function of dMn along the mixing gradient of Capelinhos, Aisics, Cypress and White Castle (2015). Free inorganic sulfides (ΣS = H<sub>2</sub>S + HS<sup>-</sup> + S<sup>2-</sup>) were measured with the CHEMINI analyzer and dissolved O<sub>2</sub> was monitored with an Optode (Aanderaa) during each sampling. Free sulfides are not available at Y3 and Sapin. The corresponding dataset is presented in **Table S3**. ΣS data can be plotted either against dMn or temperature thanks to the linear dMn-T relationship obtained at each smoker (**Figure S2**).

### 4.3. Limitation of the *in situ* filtration approach

In-situ filtration is necessary for an accurate description of the partitioning (dissolved vs particulate) of some metals such as Fe, Cu or Zn at deep sea vents. However, this method does not allow the exact quantification of the major seawater cations (e.g. Mg or Ca) in the particulate phase. This is also the case for sulfur, which, like major cations, is mainly found under dissolved forms. These chemical species correspond on one hand to sulfate ions from seawater and on the other hand to free sulfide from the hydrothermal fluid. This problem of quantification of sulfur and major cations in the particulate fraction, resulting from the above-mentioned problem of evaporation of a small volume of fluid on the filter (~200  $\mu\text{L}$ ), limits the quantification of potentially existing Ca- and Mg-bearing sulfate mineral phases such as anhydrite or caminite, respectively. Assuming that this fluid evaporation problem can be solved, we would inevitably face the additional problem of the non-stability of these mineral phases at lower temperatures (i.e. during sample retrieval). Precipitation of anhydrite is thermodynamically favorable at temperatures between 150°C and 300°C and the dissolution kinetics under 150°C is  $\sim 0.3 \text{ nM.s}^{-1}$  (Feely et al., 1987). While this rate is slow enough for part of the precipitated anhydrite to temporarily survive in the cold part of the mixing gradient, this rate is too fast to quantitatively recover this fraction from the filters that inevitably remain in contact with a cooled fluid during the few hours of sample retrieval.

## 5. Conclusion

We addressed the dissolved and particulate partitioning of Fe, Cu, Zn and Ba in the early buoyant plume (4-150°C) of black and clear smokers from the Lucky Strike vent field (MAR). All smokers displayed similar metal partitioning upon mixing. Most of Fe, Ca and Ba were measured in the dissolved fraction ( $< 0.45 \mu\text{m}$ ) whereas Cu and Zn were mainly found as particles ( $> 0.45 \mu\text{m}$ ). This is in agreement with previous findings in the close proximity of the vent orifice (Klevenz et al., 2011; Findlay et al., 2015).

A decrease of the total Fe and Cu concentrations was observed in the sampled fluids from east to west, i.e. from Capelinhos to Sapin, highlighting a spatial variability of the chemical composition of the buoyant plume throughout the vent field. This variability was not as marked for Ba and Ca. The most striking disparity of the buoyant plume chemical composition was observed between Capelinhos and the western vents from the MLSHF distributed around the fossil lava lake. However, only weak changes could be noticed for Fe and Cu between sites within the MLSHF. The variability of the chemical composition in the early mixing plume (50–150°C) between vent sites within the MLSHF seems to be mainly controlled by the end-members fluid signature. In other words, chemical changes in that part of the mixing are limited and subsurface reactions, conductive cooling or differences in channeling pathways were assumed to be the main drivers of the observed chemical composition variability.

Along the mixing gradient studied, metal sulfides were the dominant minerals species between 50 and 150 °C. Particles mainly consisted of sphalerite (or wurtzite) and Cu-Fe sulfides, in agreement with the statistically significant correlations measured between pFe, pCu, pZn concentrations. While sulfide minerals contribution progressively decreases with dilution, barite precipitation is mainly observed at temperatures in the range 10-50°C and the onset of Fe oxides precipitation is only significant in the coldest part of the gradient ( $\sim 5^\circ\text{C}$ ).

Our work provides new insights into the reactions occurring at hydrothermal vents but would have benefit from other approaches such as the study of in-situ collected particles by Raman spectroscopy (Rouxel et al., 2016; Toner et al., 2016). A specific study of nanoparticles after *in situ* filtration would also be worth undertaking since the surface reactivity of nanoparticles is much more important than those of larger particles (van Leeuwen et al., 2013). This latter observation suggests that elements adsorbed onto nanoparticles surface could be transported up to kilometers away from the vent source. Finally characterizing the spatial variability of the cold part of the chemical gradients, where vent communities thrive, will be of great interest to increase our understanding on how abiotic factors structure vent fauna habitats at the field scale (Sarrazin et al. 2015).



## Acknowledgement

We are grateful to captains and crew of the R/V Pourquoi Pas?, R/V l'Atalante and the Victor 6000 ROV for their assistance at sea, Nicolas Gayet for help in collecting samples, Julie Tourolle for the bathymetric map, Céline Liorzou, Marie-Laure Rouget and Bleuenn Gueguen (PSO) for ICP-AES and ICP-MS measurements. We are also grateful to Mathilde Cannat, Pierre-Marie Sarradin and Jérôme Blandin coordinators of the projects and PI cruises (MomarSat 2014, doi.org: 10.17600/14000300; MomarSat 2015, doi.org: 10.17600/15000200; MomarSat 2016, doi.org: 10.17600/16001200). We acknowledge financial support from the French ANR Luckyscales project (ANR-14-CE02-0008-02), the EU project EMSO (<http://www.emso-eu.org/>) and the 'Laboratoire d'Excellence' LabexMER (ANR-10-LABX-19).

## Contributions

Analyzing results and manuscript preparation (L.C and M.W.), sampling and analysis (L.C., A.L-H., V.C., C.C. and M.W.), project planning and experimental design (L.C., M.W., A.L-H., C.C, R.D.R., V.C. and P.-M. S.). All authors (L.C., V.C., E.P., A.L-H., C.C., G.D., R.D.R., P.-M. S. and M.W.) contributed to the discussion of the results and their implications, as well as commenting on the manuscript.

# References

- Alt, J. C. (1995). Subseafloor processes in Mid-Ocean Ridge hydrothermal systems. *Seafloor Hydrothermal Systems: Physical, chemical, biological, and geological interactions, Geophysical Monograph Series, 91*, 85–114.
- Barreyre, T., Escartín, J., Garcia, R., Cannat, M., Mittelstaedt, E., & Prados, R. (2012). Structure, temporal evolution, and heat flux estimates from the Lucky Strike deep-sea hydrothermal field derived from seafloor image mosaics. *Geochemistry, Geophysics, Geosystems, 13*(4), 1–29.
- Bennett, S. A., Achterberg, E. P., Connelly, D. P., Statham, P. J., Fones, G. R., & German, C. R. (2008). The distribution and stabilisation of dissolved Fe in deep-sea hydrothermal plumes. *Earth and Planetary Science Letters, 270*(3–4), 157–167.
- Breier, J. A., Toner, B. M., Fakra, S. C., Marcus, M. A., White, S. N., Thurnherr, A. M., & German, C. R. (2012). Sulfur, sulfides, oxides and organic matter aggregated in submarine hydrothermal plumes at 9°50'N East Pacific Rise. *Geochimica et Cosmochimica Acta, 88*, 216–236.
- Chavagnac, V., Leleu, T., Boulart, C., Barreyre, T., Castillo, A., Menjot, L., Cannat, M., Escartin, J., & Sarradin, P. M. (2015). Deep-sea observatory EMSO-Azores (Lucky Strike, 37°17'N, MAR) : Impact of fluid circulation pathway on chemical hydrothermal fluxes. *Abstract: AGU Fall Meeting, San Francisco (USA)*.
- Chavagnac V., Leleu T., Fontaine F., Cannat M., Ceuleneer G., Castillo A., 2018a. Spatial variations in vent chemistry at the Lucky Strike hydrothermal field, Mid Atlantic Ridge (37°N): updates for subseafloor flow geometry from the newly discovered Capelinhos vent. *G-Cubed*, doi:10.1029/2018GC007765
- Chavagnac V., Saleban Ali H., Jeandel C., Leleu T., Destigneville C., Castillo A., Cotte L., Waeles M., Cathalot C., Haes-Huon A., Nonnotte P., Sarradin P.-M., Cannat M., 2018b. Sulfate minerals control dissolved rare earth element flux and Nd isotope signature of buoyant hydrothermal plume (EMSO-Azores, 37°N Mid-Atlantic Ridge). *Chemical Geology*, doi: 10.1016/j.chemgeo.2018.09.021
- Combier, V., Seher, T., Singh, S. C., Crawford, W. C., Cannat, M., Escartín, J., & Dusunur, D. (2015). Three-dimensional geometry of axial magma chamber roof and faults at Lucky Strike volcano on the Mid-Atlantic Ridge. *Journal of Geophysical Research: Solid Earth, 120*(8), 5379–5400.
- Corliss, J. B., Dymond, J., Gordon, L. I., Edmond, J. M., von Herzen, R. P., Ballard, R. D., Green, K., Williams, D., Bainbridge, A., Crane, K., & van Andel, T. H. (1979). Submarine thermal springs on the Galapagos Rift. *Science, 203*(16), 1073–1083.
- Cotte, L., Waeles, M., Pernet-Coudrier, B., Sarradin, P. M., Cathalot, C., & Riso, R. D. (2015). A comparison of in situ vs. ex situ filtration methods on the assessment of dissolved and particulate metals at hydrothermal vents. *Deep Sea Research I, 105*, 186–194.
- Cowen, J. P., Massoth, G. J., & Feely, R. A. (1990). Scavenging rates of dissolved manganese in a hydrothermal vent plume. *Deep Sea Research A, 37*(10), 1619–1637.
- Edmond, J. M., Measures, C., Mangum, B., Grant, B., Sclater, F. R., Collier, R., Hudson, A., Gordon, L. I., & Corliss, J. B. (1979a). On the formation of metal-rich deposits at ridge crests. *Earth and Planetary Science Letters, 46*(1), 19–30.
- Edmond, J. M., Measures, C., McDuff, R. E., Chan, L. H., Collier, R., Grant, B., Gordon, L. I., & Corliss, J. B. (1979b). Ridge crest hydrothermal activity and the balances of the major and minor elements in the ocean: The Galapagos data. *Earth and Planetary Science Letters, 46*(1), 1–18.
- Edmond, J. M., Von Damm, K. L., McDuff, R. E., & Measures, C. I. (1982). Chemistry of hot springs on the East Pacific Rise and their effluent dispersal. *Nature, 297*(5863), 187–191.
- Escartin, J., Barreyre, T., Cannat, M., Garcia, R., Gracias, N., Deschamps, A., Salocchi, A., Sarradin, P. M., & Ballu, V. (2015). Hydrothermal activity along the slow-spreading Lucky Strike ridge segment (Mid-Atlantic Ridge): Distribution, heatflux, and geological controls. *Earth and Planetary Science Letters, 431*, 173–185.
- Feely, R. A., Geiselman, T. L., Baker, E. T., Massoth, G. J., & Hammond, S. R. (1990a). Distribution and composition of hydrothermal plume particles from the ASHES vent field at Axial Volcano, Juan de Fuca Ridge. *Journal of Geophysical Research: Solid Earth, 95*(B8), 12855–12873.
- Feely, R. A., Gendron, J. F., Baker, E. T., & Lebon, G. T. (1994). Hydrothermal plumes along the East Pacific Rise, 8°40' to 11°50'N: Particle distribution and composition. *Earth and Planetary Science Letters, 128*(1), 19–36.
- Feely, R. A., Lewison, M., Massoth, G. J., Robert-Baldo, G., Lavelle, J. W., Byrne, R. H., Von Damm, K. L., & Curl, H. C. (1987). Composition and dissolution of black smoker particulates from active vents on the Juan de Fuca Ridge. *Journal of Geophysical Research: Solid Earth, 92*(B11), 11347–11363.
- Feely, R. A., Massoth, G. J., Baker, E. T., Cowen, J. P., Lamb, M. F., & Kroglund, K. A. (1990b). The effect of hydrothermal processes on midwater phosphorus distributions in the northeast Pacific. *Earth and Planetary Science Letters, 96*(3), 305–318.

- 1 Feely, R. A., Trefry, J. H., Lebon, G. T., & German, C. R. (1998). The relationship between P/Fe and V/Fe ratios  
2 in hydrothermal precipitates and dissolved phosphate in seawater. *Geophysical Research Letters*, 25(13),  
3 2253–2256.
- 4 Field, M. P., & Sherrell, R. M. (2000). Dissolved and particulate Fe in a hydrothermal plume at 9°45'N, East  
5 Pacific Rise: Slow Fe (II) oxidation kinetics in Pacific plumes. *Geochimica et Cosmochimica Acta*, 64(4),  
6 619–628.
- 7 Findlay, A. J., Gartman, A., Shaw, T. J., & Luther, G. W. (2015). Trace metal concentration and partitioning in  
8 the first 1.5 m of hydrothermal vent plumes along the Mid-Atlantic Ridge: TAG, Snakepit, and Rainbow.  
9 *Chemical Geology*, 412, 117–131.
- 10 Fitzsimmons, J. N., Boyle, E. A., & Jenkins, W. J. (2014). Distal transport of dissolved hydrothermal iron in the  
11 deep South Pacific Ocean. *Proceedings of the National Academy of Sciences*, 111(47), 16654–16661.
- 12 Fitzsimmons, J. N., John, S. G., Marsay, C. M., Hoffman, C. L., Nicholas, S. L., Toner, B. M., German, C. R., &  
13 Sherrell, R. M. (2017). Iron persistence in a distal hydrothermal plume supported by dissolved-particulate  
14 exchange. *Nature Geoscience*, 10(3), 195–201.
- 15 Fontaine, F. J., Wilcock, W. S. D., & Butterfield, D. A. (2007). Physical controls on the salinity of mid-ocean  
16 ridge hydrothermal vent fluids. *Earth and Planetary Science Letters*, 257(1), 132–145.
- 17 Gartman, A., Findlay, A. J., & Luther, G. W. (2014). Nanoparticulate pyrite and other nanoparticles are a  
18 widespread component of hydrothermal vent black smoker emissions. *Chemical Geology*, 366, 32–41.
- 19 Gartman, A., & Luther, G. W. (2013). Comparison of pyrite (FeS<sub>2</sub>) synthesis mechanisms to reproduce natural  
20 FeS<sub>2</sub> nanoparticles found at hydrothermal vents. *Geochimica et Cosmochimica Acta*, 120, 447–458.
- 21 German, C. R., Campbell, A. C., & Edmond, J. M. (1991). Hydrothermal scavenging at the Mid-Atlantic Ridge:  
22 Modification of trace element dissolved fluxes. *Earth and Planetary Science Letters*, 107(1), 101–114.
- 23 German, C. R., Klinkhammer, G. P., Edmond, J. M., Mitra, A., & Elderfield, H. (1990). Hydrothermal scavenging  
24 of rare-earth elements in the ocean. *Nature*, 345(6275), 516–518.
- 25 Graham, U. M., & Ohmoto, H. (1994). Experimental study of formation mechanisms of hydrothermal pyrite.  
26 *Geochimica et Cosmochimica Acta*, 58(10), 2187–2202.
- 27 Hatta, M., Measures, C. I., Wu, J., Roshan, S., Fitzsimmons, J. N., Sedwick, P., & Morton, P. (2015). An overview  
28 of dissolved Fe and Mn distributions during the 2010–2011 US GEOTRACES north Atlantic cruises:  
29 GEOTRACES GA03. *Deep Sea Research II*, 116, 117–129.
- 30 Hawkes, J. A., Connelly, D. P., Gledhill, M., & Achterberg, E. P. (2013). The stabilisation and transportation of  
31 dissolved iron from high temperature hydrothermal vent systems. *Earth and Planetary Science Letters*,  
32 375, 280–290.
- 33 Haymon, R. M., & Kastner, M. (1981). Hot spring deposits on the East Pacific Rise at 21°N: preliminary  
34 description of mineralogy and genesis. *Earth and Planetary Science Letters*, 53(3), 363–381.
- 35 Hsu-Kim, H., Mullaugh, K. M., Tsang, J. J., Yücel, M., & Luther, G. W. (2008). Formation of Zn- and Fe-sulfides  
36 near hydrothermal vents at the Eastern Lau Spreading Center: Implications for sulfide bioavailability to  
37 chemoautotrophs. *Geochemical Transactions*, 9(1), 1–14.
- 38 Humphris, S. E., Fornari, D. J., Scheirer, D. S., German, C. R., & Parson, L. M. (2002). Geotectonic setting of  
39 hydrothermal activity on the summit of Lucky Strike Seamount (37°17'N, Mid-Atlantic Ridge).  
40 *Geochemistry, Geophysics, Geosystems*, 3(8), 1–24.
- 41 James, R. H., & Elderfield, H. (1996). Dissolved and particulate trace metals in hydrothermal plumes at the Mid-  
42 Atlantic Ridge. *Geophysical Research Letters*, 23(23), 3499–3502.
- 43 Klar, J. K., James, R. H., Gibbs, D., Lough, A., Parkinson, I., Milton, J. A., Hawkes, J. A., & Connelly, D. P.  
44 (2017). Isotopic signature of dissolved iron delivered to the Southern Ocean from hydrothermal vents in  
45 the East Scotia Sea. *Geology*, 45(4), 351–354.
- 46 Klevenz, V., Bach, W., Schmidt, K., Hentscher, M., Koschinsky, A., & Petersen, S. (2011). Geochemistry of vent  
47 fluid particles formed during initial hydrothermal fluid–seawater mixing along the Mid-Atlantic Ridge.  
48 *Geochemistry, Geophysics, Geosystems*, 12(10), 1–23.
- 49 Le Bris, N., Sarrafin, P. M., Birot, D., & Alayse-Danet, A. M. (2000). A new chemical analyzer for in situ  
50 measurement of nitrate and total sulfide over hydrothermal vent biological communities. *Marine*  
51 *Chemistry*, 72(1), 1–15.
- 52 Lê, S., Josse, J., & Husson, F. (2008). FactoMineR: An R Package for Multivariate Analysis. *Journal of Statistical*  
53 *Software*, 25(1), 1–18.
- 54 Leleu, T. (2017). Variabilité spatio-temporelle de la composition des fluides hydrothermaux (Observatoire Fond  
55 de Mer EMSO-Açores, Lucky Strike): Traçage de la circulation hydrothermale et quantification des flux  
56 chimiques associés. *PhD thesis, Université de Toulouse, Toulouse, France*.
- 57 Leleu, T., Chavagnac, V., Cannat, M., Fontaine, F. J., Ceuleneer, G., & Castillo, A. (submitted). Spatial variations  
58 in vent chemistry at the Lucky Strike hydrothermal field, Mid Atlantic Ridge (37°N): Implications for  
59 subseafloor flow geometry. *Submitted to Geochimica et Cosmochimica (Ref: GCA-D-16-00566)*.

- 1 Leleu, T., Chavagnac, V., Castillo, A., Cannat, M., & Menjot, L. (2015). Fluid chemistry of the Capelinhos vent  
2 site: A key to understand Lucky Strike hydrothermal vent field (37°N, Mid-Atlantic Ridge). *Abstract:*  
3 *AGU Fall Meeting, San Francisco (USA)*.
- 4 McDuff, R. E., & Edmond, J. M. (1982). On the fate of sulfate during hydrothermal circulation at mid-ocean  
5 ridges. *Earth and Planetary Science Letters*, 57(1), 117–132.
- 6 Metz, S., & Trefry, J. H. (2000). Chemical and mineralogical influences on concentrations of trace metals in  
7 hydrothermal fluids. *Geochimica et Cosmochimica Acta*, 64(13), 2267–2279.
- 8 Millero, F. J., Sotolongo, S., & Izaguirre, M. (1987). The oxidation kinetics of Fe(II) in seawater. *Geochimica et*  
9 *Cosmochimica Acta*, 51(4), 793–801
- 10 Mills, R. A., Teagle, D. A. H., & Tivey, M. K. (1998). *Fluid mixing and anhydrite precipitation within the TAG*  
11 *mound* (Vol. 158). Presentation made at the Proceedings of the ocean drilling program: Scientific results, The  
12 Program, 119.
- 13 Mottl, M. J., & McConachy, T. F. (1990). Chemical processes in buoyant hydrothermal plumes on the East Pacific  
14 Rise near 21°N. *Geochimica et Cosmochimica Acta*, 54(7), 1911–1927.
- 15 Nishioka, J., Obata, H., & Tsumune, D. (2013). Evidence of an extensive spread of hydrothermal dissolved iron  
16 in the Indian Ocean. *Earth and Planetary Science Letters*, 361, 26–33.
- 17 Pester, N. J., Ding, K., & Seyfried, W. E. (2015). Vapor–liquid partitioning of alkaline earth and transition metals  
18 in NaCl-dominated hydrothermal fluids: An experimental study from 360 to 465°C, near-critical to halite  
19 saturated conditions. *Geochimica et Cosmochimica Acta*, 168, 111–132.
- 20 Pester, N. J., Reeves, E. P., Rough, M. E., Ding, K., Seewald, J. S., & Seyfried, W. E. (2012). Subseafloor phase  
21 equilibria in high-temperature hydrothermal fluids of the Lucky Strike Seamount (Mid-Atlantic Ridge,  
22 37°17'N). *Geochimica et Cosmochimica Acta*, 90, 303–322.
- 23 Reeves, E. P., McDermott, J. M., & Seewald, J. S. (2014). The origin of methanethiol in midocean ridge  
24 hydrothermal fluids. *Proceedings of the National Academy of Sciences*, 111(15), 5474–5479.
- 25 Resing, J. A., Sedwick, P. N., German, C. R., Jenkins, W. J., Moffett, J. W., Sohst, B. M., & Tagliabue, A. (2015).  
26 Basin-scale transport of hydrothermal dissolved metals across the South Pacific Ocean. *Nature*,  
27 523(7559), 200–203.
- 28 Rickard, D. (1997). Kinetics of pyrite formation by the H<sub>2</sub>S oxidation of iron (II) monosulfide in aqueous solutions  
29 between 25 and 125°C: The rate equation. *Geochimica et Cosmochimica Acta*, 61(1), 115–134.
- 30 Rona, P. A., & Trivett, D. A. (1992). Discrete and diffuse heat transfer at Ashes vent field, Axial Volcano, Juan  
31 de Fuca Ridge. *Earth and Planetary Science Letters*, 109(1), 57–71.
- 32 Rose, A. W. (1961). The iron content of sphalerite from the Central District, New Mexico and the Bingham  
33 District, Utah. *Economic Geology*, 56(8), 1363–1384.
- 34 Roshan, S., Wu, J., & Jenkins, W. J. (2016). Long-range transport of hydrothermal dissolved Zn in the tropical  
35 South Pacific. *Marine Chemistry*, 183, 25–32.
- 36 Rouxel, O., Toner, B. M., Manganini, S. J., & German, C. R. (2016). Geochemistry and iron isotope systematics  
37 of hydrothermal plume fall-out at East Pacific Rise 9°50'N. *Chemical Geology*, 441, 212–234.
- 38 Rudnicki, M. D., & Elderfield, H. (1993). A chemical model of the buoyant and neutrally buoyant plume above  
39 the TAG vent field, 26°N, Mid-Atlantic Ridge. *Geochimica et Cosmochimica Acta*, 57(13), 2939–2957.
- 40 Saito, M. A., Noble, A. E., Tagliabue, A., Goepfert, T. J., Lamborg, C. H., & Jenkins, W. J. (2013). Slow-spreading  
41 submarine ridges in the South Atlantic as a significant oceanic iron source. *Nature Geoscience*, 6(9), 775–  
42 779.
- 43 Sander, S. G., Koschinsky, A., Massoth, G., Stott, M., & Hunter, K. A. (2007). Organic complexation of copper  
44 in deep-sea hydrothermal vent systems. *Environmental Chemistry*, 4(2), 81–89.
- 45 Sands, C. M., Connelly, D. P., Statham, P. J., & German, C. R. (2012). Size fractionation of trace metals in the  
46 Edmond hydrothermal plume, Central Indian Ocean. *Earth and Planetary Science Letters*, 319–320, 15–  
47 22.
- 48 Sarradin, P. M., Lannuzel, D., Waeles, M., Crassous, P., Le Bris, N., Caprais, J. C., Fouquet, Y., Fabri, M. C., &  
49 Riso, R. (2008). Dissolved and particulate metals (Fe, Zn, Cu, Cd, Pb) in two habitats from an active  
50 hydrothermal field on the EPR at 13°N. *Science of The Total Environment*, 392(1), 119–129.
- 51 Sarradin, P. M., Sarrazin, J., Allais, A. G., Almeida, D., V., B., Boetius, A., Buffier, E., Coiras, E., Colaco, A.,  
52 Cormack, A., Dentrecolas, S., Desbruyeres, D., Dorval, P., du Buf, H., Dupont, J., Godfroy, A., Gouillou,  
53 M., Gronemann, J., Hamel, G., Hamon, M., Hoge, U., Lane, D., Le Gall, C., Leroux, D., Legrand, J.,  
54 Leon, P., Leveque, J. P., Masson, M., Olu, K., Pascoal, A., Sauter, E., Sanfilippo, L., Savino, E.,  
55 Sebastiao, L., Santos, R. S., Shillito, B., Simeoni, P., Schultz, A., Sudreau, J. P., Taylor, P., Vuillemin,  
56 R., Waldmann, C., Wenzhöfer, F., & Zal, F. (2007). EXtreme ecosystem studies in the deep OCEan:  
57 Technological developments. *Ieee*, 1–3.
- 58 Sarrazin J., Legendre P., De Busserolles F., Fabri M.-C., Guilini K., Ivanenko V. N., Morineaux M., Vanreusel  
59 A., Sarradin P.-M. (2015). Biodiversity patterns, environmental drivers and indicator species on a High-

- temperature Hydrothermal edifice, mid-Atlantic ridge. *Deep-sea Research Part II-topical Studies In Oceanography*, 121, 177–192.
- Seyfried, W. E., & Ding, K. (1995). Phase equilibria in seafloor hydrothermal systems: A review of the role of redox, temperature, pH and dissolved Cl on the chemistry of hot spring fluids at Mid-Ocean Ridges. In *Seafloor Hydrothermal Systems: Physical, Chemical, Biological, and Geological Interactions* (Vol. 91). American Geophysical Union, 248–272.
- Singh, S. C., Crawford, W. C., Carton, H., Seher, T., Combier, V., Cannat, M., Canales, J. P., Düşünür, D., Escartin, J., & Miranda, J. M. (2006). Discovery of a magma chamber and faults beneath a Mid-Atlantic Ridge hydrothermal field. *Nature*, 442(7106), 1029–1032.
- Toner, B. M., Fakra, S. C., Manganini, S. J., Santelli, C. M., Marcus, M. A., Moffett, J. W., Rouxel, O., German, C. R., & Edwards, K. J. (2009). Preservation of iron(II) by carbon-rich matrices in a hydrothermal plume. *Nature Geoscience*, 2(3), 197–201.
- Toner, B. M., Rouxel, O. J., Santelli, C. M., Bach, W., & Edwards, K. J. (2016). Iron transformation pathways and redox micro-environments in seafloor sulfide-mineral deposits: Spatially resolved Fe XAS and  $\delta(57/54)\text{Fe}$  observations. *Frontiers in Microbiology*, 7, 648.
- Trocine, R. P., & Trefry, J. H. (1988). Distribution and chemistry of suspended particles from an active hydrothermal vent site on the Mid-Atlantic Ridge at 26°N. *Earth and Planetary Science Letters*, 88(1–2), 1–15.
- van Leeuwen, H. P., Buffle, J., Duval, J. F. L., & Town, R. M. (2013). Understanding the extraordinary ionic reactivity of aqueous nanoparticles. *Langmuir*, 29(33), 10297–10302.
- Von Damm, K. L., Edmond, J. M., Grant, B., Measures, C. I., Walden, B., Weiss (1985). Chemistry of submarine hydrothermal solutions at 21°N, East Pacific Rise. *Geochimica and Cosmochimica Acta*, 49, 2197–2220.
- Von Damm, K. L., Oosting, S. E., Kozlowski, R., Buttermore, L. G., Colodner, D. C., Edmonds, H. N., Edmond, J. M., & Grebeier, J. M. (1995). Evolution of East Pacific Rise hydrothermal vent fluids following a volcanic eruption. *Nature*, 375, 47–50.
- Vuillemin, R., Le Roux, D., Dorval, P., Bucas, K., Sudreau, J. P., Hamon, M., Le Gall, C., & Sarradin, P. M. (2009). CHEMINI: A new in situ CHEmical MINIaturized analyzer. *Deep Sea Research I*, 56(8), 1391–1399.
- Waeles, M., Cotte, L., Pernet-Coudrier, B., Chavagnac, V., Cathalot, C., Leleu, T., Laës-Huon, A., Perhirin, A., Riso, R. D., & Sarradin, P.-M. (2017). On the early fate of hydrothermal iron at deep-sea vents: A reassessment after in-situ filtration. *Geophysical Research Letters*, 1–8.
- Yeats, P. A., Dalziel, J. A., & Moran, S. B. (1992). A comparison of dissolved and particulate Mn and Al distributions in the Western North-Atlantic. *Oceanologica acta*, 15(6), 609–619.
- Yücel, M., Gartman, A., Chan, C. S., & Luther, G. W. (2011). Hydrothermal vents as a kinetically stable source of iron-sulphide-bearing nanoparticles to the ocean. *Nature Geoscience*, 4(6), 367–371.
- Zheng, X.-Y., Plancherel, Y., Saito, M. A., Scott, P. M., & Henderson, G. M. (2016). Rare earth elements (REEs) in the tropical South Atlantic and quantitative deconvolution of their non-conservative behavior. *Geochimica et Cosmochimica Acta*, 177, 217–237.

